

# Integrated feature scale modeling of plasma processing of porous and solid SiO<sub>2</sub>. II. Residual fluorocarbon polymer stripping and barrier layer deposition

Arvind Sankaran<sup>a)</sup>

*Department of Chemical and Biomolecular Engineering, University of Illinois, 1406 W. Green St., Urbana, Illinois 61801*

Mark J. Kushner<sup>b)</sup>

*Department of Electrical and Computer Engineering, University of Illinois, 1406 W. Green St., Urbana, Illinois 61801*

(Received 15 January 2004; accepted 3 May 2004; published 14 July 2004)

The adoption of low dielectric constant materials as inter-level dielectrics in microelectronics fabrication will ultimately depend on process integration. Porous SiO<sub>2</sub> (PS) is one candidate material. Cleaning of residual polymer from trenches following etching using fluorocarbon plasmas and the deposition of a continuous barrier layer are critical processes for integration of PS as inter-level dielectrics. To investigate these issues, reactions mechanisms for plasma stripping of fluorocarbon polymer using oxygen containing plasmas and deposition of metal barrier coatings into PS trenches were developed, and incorporated into a feature profile model. The reaction mechanism was validated by comparison to experiments for blanket plasma etching of polytetrafluoroethylene using Ar–O<sub>2</sub> chemistries. Plasma stripping of fluorocarbon polymers from solid SiO<sub>2</sub> (SS) trenches was found to be less efficient at higher aspect ratios. Stripping was also less efficient from PS trenches having large average pore radius and high interconnectivity. Cu ionized metal physical vapor deposition was investigated as a surrogate for barrier coating in SS and PS trenches. Compared to SS, thin film deposition was less conformal for PS having closed pore networks. Thicker films were required for interconnected PS to avoid pin-hole formation. © 2004 American Vacuum Society. [DOI: 10.1116/1.1764822]

## I. INTRODUCTION

Copper interconnect wiring and low dielectric constant (low-*k*) materials as inter-level dielectrics are being implemented to reduce the resistance-capacitance propagation delay in microelectronic devices.<sup>1</sup> The successful integration and reliability of low-*k* dielectrics as inter-level dielectrics depends in part on their compatibility with current processing techniques.<sup>2</sup> The main process steps of interest are photoresist exposure and development, plasma etching to define vias and trenches, cleaning of the feature, and the deposition of barrier coating and seed layers for subsequent electrochemical deposition. For example, post etch cleaning of trenches and vias reduces the contact resistance between the plasma-exposed surfaces and the subsequent deposited metal layers.<sup>3</sup> With organic low-*k* dielectric materials, which are etched using oxygen containing plasmas, there is often a residual oxidized layer on the surface which is typically cleaned by argon sputtering.<sup>4</sup> Inorganic low-*k* dielectrics, such as porous SiO<sub>2</sub> (PS), are typically etched using fluorocarbon plasma chemistries. The residual fluorocarbon polymer remaining after etching and the photoresist are typically removed using O<sub>2</sub> based chemistries (among others).<sup>5–7</sup>

Plasma etching of silicon based dielectrics is usually performed using fluorocarbon chemistries and proceeds through

the formation of steady state fluorocarbon polymer layer on the top of the dielectric surface.<sup>8</sup> This polymer layer determines the etch rates, selectivity and the morphology of the profile.<sup>9</sup> If the polymer is not totally removed prior to the subsequent metal deposition for a barrier coating or seed layer, the sputtered metal atoms could mix with the polymer to form a high resistance material and thus increase the contact resistance. The formation of this high resistance material also raises reliability concerns.<sup>10</sup> The residual polymer results in defects at metal–Si interfaces leading to a high leakage current.<sup>3</sup> As a result, the removal of these residues is critical for device integration.

Several wet and dry methods for cleaning fluorocarbon residues, which typically involve oxidizing chemistries, have been previously investigated.<sup>5,10–14</sup> Wet cleaning methods include RCA cleans, HF dips, H<sub>2</sub>SO<sub>4</sub>–H<sub>2</sub>O<sub>2</sub> and amine based solvents.<sup>3</sup> However with decreases in feature sizes, wet strip processes have been found to be less effective.<sup>15</sup> As an alternative to wet stripping, plasma cleaning methods have been extensively investigated.<sup>15,16</sup> Oxygen plasmas are typically used and are efficient in stripping residual polymer from solid SiO<sub>2</sub> (SS). Remote oxygen plasmas are often preferred with the goal of minimizing plasma damage.<sup>5</sup> The removal of organic polymer using oxygen plasmas has other widespread applications in semiconductor processing as well. For example, Ar–O<sub>2</sub> chemistries are widely used for lithography in processes such as resist thinning. This technique is useful in reducing the gate length without increasing the complexity of the lithography.<sup>17,18</sup> Photoresist ashing is also performed

<sup>a)</sup>Present address: Novellus Systems, 11155 SW Leveton Dr., Tualatin, OR 97062; electronic mail: arvind.sankaran@novellus.com.

<sup>b)</sup>Author to whom correspondence should be addressed; electronic mail: mjk@uiuc.edu

using  $O_2$  chemistries.<sup>19</sup>  $O_2$  based chemistries also find applications in the etching of organic and hybrid low- $k$  dielectrics, which are patterned using  $SiO_2$  or  $SiN_x$  hardmasks.<sup>20,21</sup>

There are potential drawbacks to using  $O_2$  plasmas for cleaning of low- $k$  PS materials such as methyl silsesquioxane and hydrogen silsesquioxane.<sup>4</sup> Typically  $O_2$  plasmas oxidize these materials into a  $SiO_2$ -like material which increases their dielectric constants.<sup>7</sup> As a result other stripping techniques which use  $H_2$  containing or  $NF_3$ -Ar chemistries are being considered.<sup>14,15,22</sup>

Post etch processing of inter-level dielectrics also involves deposition of thin metal barrier and seed layers following the residual polymer cleaning and preceding the final metallization.<sup>23,24</sup> The deposition of thin films on porous materials is challenging as the pore morphology may have significant effects on the functionality, conformality and reliability of the capping barrier and metal seed layers.<sup>25</sup> Deposition of such thin barrier and seed films are typically achieved by means of physical vapor deposition, chemical vapor deposition or atomic layer deposition.<sup>25,26</sup>

During the deposition of thin films onto meso-connected (interconnected) porous networks, the deposition of reactants into the entry of pore chains is inefficient, which could result in an exposed pore being unabridged, a phenomenon referred to as creation of pin holes.<sup>2</sup> Meso-connectivities have dimensions (2–20 nm) which are comparable to the average pore radius. Micro-connectivity (closed pores) consists of atomic level connectivities inherent to the material and whose dimensions (a few Å) are typically small in comparison to the average pore radius. As such, pinholes due to atomic level connectivities are typically not a problem. For example deposition of TaN barrier coating using physical vapor deposition onto a methyl silsesquioxane based film with meso-connectivities and average pore radius 3–5 nm was found to have pinholes, which were detected by an increase in the sheet resistance.<sup>25</sup> A partially porous diffusion barrier can also lead to contamination during the subsequent metallization process.<sup>27</sup> During thin film deposition onto interconnected porous substrates using chemical vapor deposition and atomic layer deposition, the precursors can penetrate and deposit material through the entire porous network, which also affects the integrity of the film.<sup>26</sup> As a result, sealing of interconnected pore networks and conformal barrier layer deposition onto closed pore networks are important to the implementation of PS as inter-level dielectrics.

In this article, we present results from a computational investigation of post etch processing, [residual fluorocarbon stripping and ionized metal physical vapor deposition (IMPVD)] of SS and PS films etched in fluorocarbon plasmas. The study was performed using the Monte Carlo Feature Profile Model (MCFPM), which has been modified to address two-phase porous materials.<sup>28,29</sup> This model is described in detail in the companion publication, Part I, cited as Ref. 30. The MCFPM uses energy and angular distributions of reactants obtained from the Hybrid Plasma Equipment Model (HPEM).<sup>31,32</sup> A surface reaction mechanism for etching of fluorocarbon polymers in  $O_2$  plasma was developed

and applied to the stripping of residual fluorocarbon from etched PS films. The surface reaction mechanism was validated for etching of polytetrafluoroethylene (PTFE) in Ar- $O_2$  chemistries by comparison to experiments.<sup>21</sup> Using algorithms developed earlier for trench filling in nonporous films, copper IMPVD was then investigated as a surrogate for deposition of barrier coatings or seed layers into PS trenches.<sup>31</sup>

Based on experimental trends, we found that there is little fluorocarbon polymer etching in the absence of simultaneous O atom and energetic ion bombardment and our reaction mechanism reflects that. Stripping was found to be less effective for interconnected PS films with larger average pore radii and larger porosities due to there being unfavorable view angles to the incident energetic fluxes. This effect was more pronounced for vias and trenches having high large aspect ratios. Unfavorable view angles also resulted in non-conformal metal deposition in closed pore networks and creation of pinholes in interconnected networks during Cu IMPVD.

The HPEM and the MCFPM are briefly discussed in Sec. II. The surface reaction mechanism for oxygen etching of organic polymer is discussed in Sec. III followed by validation of the mechanism, which is presented in Sec. IV. Stripping of residual fluorocarbon from high aspect ratio trenches of PS and SS using  $O_2$  plasmas is discussed in Sec. V. Copper IMPVD as a surrogate to deposition of barrier coating and seed layer onto the cleaned trenches is presented in Sec. VI, followed by concluding remarks in Sec. VII.

## II. DESCRIPTION OF THE MODELS

### A. Reactor scale models

The HPEM has been previously described and so is only briefly summarized here.<sup>32,33</sup> The HPEM is a two-dimensional simulator which iteratively achieves a quasi-steady state solution. The main modules are the Electromagnetic Module, the Electron Energy Transport Module and the Fluid Kinetics Module. Electromagnetic and magneto-static fields are calculated in the Electromagnetics Module. These fields are then used in the Electron Energy Transport Module to obtain electron impact source functions and transport coefficients by either solving the electron energy equation or by a Monte Carlo simulation. These results are then passed to the Fluid Kinetics Module, in which separate continuity, momentum and energy equations are solved for ions and neutral species. Poisson's equation is solved for the time varying electrostatic potential throughout the reactor. Output from Fluid Kinetics Module (densities and electrostatic fields) is then transferred to the other modules and the process is iterated until a converged solution is obtained.

The Plasma Chemistry Monte Carlo Module (PCMCM) in the HPEM produces the energy and angular distributions for neutrals and ions striking the wafer surface.<sup>31</sup> The PCMCM is typically executed at the end of the HPEM after species densities, fluxes and electric properties have converged. The PCMCM launches pseudoparticles representing ions and neutrals based on the electron impact source func-

tions and the time dependent electric fields obtained from the HPEM. Using a Monte Carlo simulation, the PCMCM tracks the trajectories of the ions and neutrals and captures its gas phase collisions and interactions with the surface. The gas-phase collisions are based on the chemistry used in the HPEM and surface interactions are represented by reactive sticking coefficients. Statistics are collected over multiple launchings of the pseudoparticles. The PCMCM produces energy and angular distributions of neutrals and ions at specified locations on all surfaces. The MCFPM uses these distributions at the wafer to predict etch profiles.

## B. Feature scale model

The MCFPM has been previously described and so is briefly summarized here.<sup>28–30</sup> The fluxes of reactant species and their energy and angular distributions from the PCMCM are inputs to the MCFPM. The MCFPM resolves the surface (mask, photoresists, semiconductors) of the wafer using a two-dimensional rectilinear mesh. Each cell in the mesh is assigned a material identity. Gas phase species are represented by pseudoparticles and surface species are represented by computational mesh cells. Pseudo-particles are launched towards the surface from random locations above the trench with energies and angles sampled from the energy and angular distributions obtained from the PCMCM. The trajectories of the pseudoparticles are tracked until they hit a surface, where a generalized surface reaction mechanism controls the interaction. The reaction mechanism is ultimately expressed as a probability array for the reaction between the pseudoparticle plasma species and the surface species. When a pseudoparticle hits the surface, a reaction is chosen based on these probability arrays using Monte Carlo techniques. Based on the selected reactions, the identities of the mesh cells change representing reaction products. Material is added or removed constituting a reaction product. Gas-phase species evolving from these reactions are tracked as new gas phase pseudoparticles.

The interaction of energetic particles with surface species determined by the angular and energy dependence is discussed in detail in Part I and is summarized here.<sup>30</sup> Ions neutralize upon interaction with the surface and are not distinguished from energetic neutrals. The generalized reaction probability for a particle of energy  $E$  incident onto a surface at an angle  $\theta$  from the vertical is<sup>34,35</sup>

$$p(\theta) = p_0 \left[ \frac{E^n - E_t^n}{E_r^n - E_t^n} \right] f(\theta), \quad (1)$$

where  $E_t$  is the threshold energy of the process,  $E_r$  is a reference energy, and  $p_0$  is the probability for normal incidence at  $E_r$ ,  $f(\theta)$  is the relative probability at angle of incidence  $\theta$ . We have modeled  $f(\theta)$  as a semiempirical function, typical of chemically enhanced sputtering with a maximum value near  $\theta = 60^\circ$ .<sup>35</sup> The dependence of etch yield on angle in fluorocarbon plasmas is discussed in Part I.<sup>30</sup>

Reflection of energetic particles from surfaces can be either specular or diffusive. The energy loss is large for diffusive scattering and small for specular. To account for surface

roughness on spatial scales not resolved by our model, we specified that a fraction  $f_d = 0.25$  was diffusively scattered. The energy of specularly reflected particle was scaled such that forward scattered particles retain the majority of their energy. The specularly reflected particle energy for incident energy  $E_I$  is

$$E_s(\theta) = E_I \left( \frac{E_I - E_c}{E_{ts} - E_c} \right) \left( \frac{\theta - \theta_c}{90^\circ - \theta_c} \right) \quad (2)$$

for  $\theta > \theta_c$ ,  $E_c < E_I < E_{ts}$ . Particles having  $\theta < \theta_c$  or  $E_I < E_c$  are said to diffusively scatter. Particles having  $E_I > E_{ts}$  are said to retain all of their energy subject to the angular correction. We used  $E_{ts} = 100$  eV,  $E_c = 0$  eV, and  $\theta_c = 60^\circ$ . The final reflected energy of the particle is a weighted sum of the specularly reflected energy and diffusively reflected energy.

The MCFPM is also capable of addressing surface diffusion during deposition of materials. We used this option only for diffusion of metal atoms on metal underlayers. The diffusion algorithm for Cu IMPVD has been described earlier and is summarized here.<sup>31</sup> All depositing metal atoms are first physisorbed and are treated differently from the underlying material even if they have the same composition. The physisorbed atoms diffuse on the surface before they are chemisorbed onto the underlying material. An adsorbed cell can diffuse into any unoccupied adjacent cell in the mesh. The probability that an adsorbed cell  $i$  moves to another cell  $j$  depends on their relative potential energies, which are based on effective Morse potentials:

$$\Phi_{ij} = \Phi_0 \left\{ \exp\left(-2 \frac{r_{ij} - r_0}{a_0}\right) - 2 \exp\left(-\frac{r_{ij} - r_0}{a_0}\right) \right\}, \quad (3)$$

where  $r_{ij}$  is the distance between the center of the cells.  $\Phi_0$  was set to 0.3 eV based on the predictions by Lu *et al.*<sup>31</sup>  $r_0$  and  $a_0$  were set to 1.6 and 5 nm based on mesh scale lengths as opposed to atomic lengths. The probability of diffusion to all possible locations is summed and normalized. The final diffusion path is then randomly chosen. Based on the chosen value of the activation energy for diffusion from  $i$  to  $j$  ( $E_{ij}$ ), the adsorbed cell either chemisorbs or diffuses. The frequency of such trials is governed by the jump frequency  $\nu$ ,

$$\nu = -\nu_{ij} \ln(r), \quad (4)$$

where

$$\nu_{ij} = \nu_0 \exp\left(-\frac{E_{ij}}{k_b T_s}\right) \quad (5)$$

and

$$\nu_0 = 2k_b T_s / h, \quad (6)$$

where  $h$  is Planck's constant,  $k_b$  is Boltzmann's constant, and  $T_s$  is the substrate temperature. At 393 K,  $\nu_0 = 1.6 \times 10^{12} \text{ s}^{-1}$ . Based on the specified threshold jump frequency ( $\nu_t$ ), the cell chemisorbs if  $\nu < \nu_t$ .  $\nu_t$  was chosen to be  $10^8 \text{ s}^{-1}$  based on earlier studies.<sup>31</sup>

PS is modeled as stoichiometric SiO<sub>2</sub> with vacuum pores. The pore radii and locations are randomly chosen and distributed in the numerical mesh used by the MCFPM with a Gaussian distribution of radii having probability

$$p(r) \sim \exp(-((r-r_0)/\Delta r)^2), \quad (7)$$

where  $r$  is the radius of the incorporated pore,  $r_0$  is the average pore radius, and  $\Delta r$  is the standard deviation. Algorithms were developed to include the capability of creating both closed and interconnected pore networks.<sup>30</sup> The interconnectivity of the network is the fraction of pores that are connected to another pore. PS having an interconnectivity of 0% consists of isolated pores. In PS having an interconnectivity of 100% every pore is connected to at least one other pore in a low fractal dimension manner.

### III. SURFACE REACTION MECHANISMS

#### A. Etching of Si and SiO<sub>2</sub> in fluorocarbon plasmas

The reaction mechanism for etching Si and SiO<sub>2</sub> in CHF<sub>3</sub>, C<sub>2</sub>F<sub>6</sub>, or C<sub>4</sub>F<sub>8</sub> plasmas is extensively discussed in Ref. 30. Briefly, fluorocarbon radicals produced by electron impact of the feedstock gases deposit a thin (2–5 nm) polymer layer on the Si or SiO<sub>2</sub> surface. The deposition process is enabled by low energy ion activation of surface sites. The fluorocarbon thickness regulates the delivery of activation energy and reactants to the interface between the polymer and substrate. When activated by ion bombardment, the oxygen in the SiO<sub>2</sub> reacts with carbon groups in the polymer to release COF<sub>x</sub> etch products; while the Si in the SiO<sub>2</sub> reacts with F in the polymer to release SiF<sub>x</sub>. This process consumes both the substrate and the polymer. Si, having no oxygen, reacts less rapidly with the polymer, resulting in a thicker polymer layer which reduces the rate of activation to the polymer–Si interface. The end result is a lower etch rate for Si. Energetic ion bombardment can also sputter the polymer. The important scalings for this study are that polymer deposition relies on isotropic neutral fluxes and low energy activation (<10s eV), either by ions or reflected neutrals, which may also have broad angular distributions. Direct sputtering of polymer relies on energetic fluxes of ions and reflected neutrals (>10s eV) which tend to be more anisotropic.

#### B. Etching of organic polymer

The removal of organic polymer using plasmas has widespread applications and has been extensively characterized. Early applications include reactive ion etching of organic material in multilevel resist systems in an oxygen plasma.<sup>36,37</sup> Recent applications are the removal of organic contaminants and residual polymers following fluorocarbon etching.<sup>6,7</sup> O<sub>2</sub> plasmas are also being investigated for patterning organic low- $k$  dielectrics. Investigations on the mechanisms concentrate on the contribution of the major reactive species O<sub>2</sub>(<sup>1</sup>Δ), O(<sup>4</sup>S), O(<sup>1</sup>D), O<sup>+</sup>, and O<sub>2</sub><sup>+</sup>.<sup>38,39</sup> The effectiveness of removal of organic material in both fluorocarbon and hydrocarbon polymers by O<sub>2</sub> plasmas is due to the

reaction of oxygen with the carbon in the polymer. This results in the breaking of the C–F and C–H bonds in the polymer and in the formation of volatile byproducts such as H<sub>2</sub>O and CO<sub>x</sub> for hydrocarbon polymers and COF<sub>x</sub>, CO<sub>x</sub>, and F<sub>x</sub> for fluorocarbon polymers.<sup>36</sup>

In high-pressure (0.5–5 Torr) oxygen discharges, O atoms are the primary etchant species.<sup>40,41</sup> Etching by O radicals was found to be thermally activated with an activation energy of 0.25–0.5 eV for a variety of organic materials such as poly-methyl-metha-acrylate (PMMA) and a phenol formaldehyde based photoresist (AZ 1350J, Shipley Co.).<sup>40,41</sup> The substrates are typically heated to 100s °C. Similar trends are found in low-pressure reactive ion etching of polyimide in Ar–O<sub>2</sub> plasma, where, for example, Selwyn reported that the O radicals are the main etchant specie.<sup>42</sup> Harper *et al.* investigated etching of polyimide by Ar<sup>+</sup> and O<sub>2</sub><sup>+</sup> beams.<sup>43</sup> They found that the etching was six times slower using the Ar<sup>+</sup> ion beam, differences attributed to increased activation by the neutral O radicals on the surface sites. Similarly low etch rates were observed in pure O<sub>2</sub> plasmas with low ion activation. For example, Egitto *et al.* observed little etching of polyimide in pure O<sub>2</sub> plasmas when they shielded the polymer from ion bombardment allowing only diffusion of radicals and thermal ions to the polymer surface.<sup>44</sup> When polymer films are exposed to such oxygen discharges without ion bombardment, their top surfaces are oxidized, creating a passivation layer, which stops further etching.

These observations suggest an ion-assisted mechanism for the etching of organic materials. Greer *et al.* observed that the etching of photoresist by an oxygen ion beam is limited by the availability of O radicals at low pressures and by ions at higher pressures.<sup>19</sup> In modeling of this etch mechanism Baggerman *et al.* proposed a similar process.<sup>37</sup> Steinbruchel *et al.* suggested a surface-damage promoted etching mechanism, where the ion impact creates a damaged surface with higher reactivity, which on subsequent attack by neutrals release the etch products.<sup>36</sup> Joubert *et al.* suggested an alternate reaction pathway where oxygen radicals first adsorb on the polymer surface. The etch reaction is then completed by activation by energetic ions.<sup>45</sup>

Based on these observations and the suggested reaction pathway by Joubert *et al.*,<sup>45</sup> we modeled the fluorocarbon polymer etch mechanism as a two-step ion-assisted process. Oxygen atoms first react with the polymer to produce an activated polymer site. Upon delivery of activation energy by ions, the activated polymer complex evolves volatile etch products.



where P<sub>s</sub> is the polymer, P<sub>s</sub><sup>\*</sup> is the activated polymer complex, I<sub>g</sub><sup>+</sup> is the ion, I<sub>h</sub> is a hot neutral, O is the etchant, and COF<sub>x</sub> is the volatile gas product. The subscripts  $s$  and  $g$  denote surfaces and gas-phase species. The polymer surface can also be directly sputtered by ions to release nonoxygen containing volatile etch products such as CF<sub>x</sub> with an energy dependence governed by Eq. (1). The threshold energy and

TABLE I. Surface reaction mechanism for oxygen plasma etching of fluorocarbon polymer and photoresists.

Species	Symbol				
Fluorocarbon polymer	P				
Photoresist	R				
Activated species	*				
Ion	$I^+$				
Gas phase species	g				
Hot neutral	$I_h$				
Surface specie	s				

Reaction <sup>a,b</sup>	$p_0$	$E_{th}(eV)$	$E_r(eV)$	$n$	Ref.
$P_s + O_g \rightarrow P_s^*$	0.50				
$P_s^* + I_g^+ \rightarrow COF_{xg} + I_h$	0.03	45	100	0.4	Eq. (1)
$P_s + I_g^+ \rightarrow CF_{xg} + I_h$	0.15	70	140	0.97	Eq. (1)
$R_s + O_g \rightarrow R_s^*$	0.01				
$R_s^* + I_g^+ \rightarrow COF_{xg} + I_h$	0.30	100	500	0.8	Eq. (1)
$R_s + I_g^+ \rightarrow CF_{xg} + I_h$	0.20	100	500	0.8	Eq. (1)

<sup>a</sup>Reactions for  $I_g^+$  are generic for all ions. All ions return to the plasma as hot neutrals. Hot neutrals have the same mechanism as ions.

<sup>b</sup>In reactions with no chemical change, the gas species are reflected from the surface. These reactions are not shown in the table.

probability for this reaction are based on the reaction mechanism developed for ion sputtering of the fluorocarbon polymer formed during etching of SS. Photoresist was modeled similar to the fluorocarbon polymer. The reaction mechanisms for oxygen etching of fluorocarbon polymer and a generic photoresist are in Table I.

### C. Cu ionized metal PVD

The surface reaction mechanism used for Cu IMPVD has been discussed earlier and is listed in Table II.<sup>31</sup> The primary ions,  $Ar^+$  and  $Cu^+$ , sputter Cu and  $SiO_2$  surfaces with an energy dependence given by Eq. (1). The angular dependence of sputtering has an energy dependence similar to chemically enhanced sputtering reaction with a maximum near  $\approx 60^\circ$ . Specular reflection, as given by Eq. (2) has  $E_c = 0$  eV and  $\theta_c = 70^\circ$ . In addition to sputtering, deposition also occurs with  $Cu^+$  bombardment. All ions not deposited are converted to hot neutrals at the surface and are treated similarly to ions in the reaction mechanism. Cu ground state

and  $Cu^*$  [ $Cu(^2D_{5/2})$ ] deposit on  $SiO_2$  and Cu surfaces. The sticking probability of Cu and  $Cu^*$  was estimated to be 0.70 on  $SiO_2$  and 0.95 on Cu.

## IV. VALIDATION OF THE REACTION MECHANISM

### A. Basic mechanism

The validation of the surface reaction mechanism for etching of SS and PS in fluorocarbon plasmas is discussed in Ref. 30. The validation for the reaction mechanism for IMPVD of Cu is discussed in Ref. 31. The reaction mechanism for  $Ar-O_2$  plasma etching of organic polymer was calibrated and validated by comparison to experiments by Standaert *et al.* for etching of PTFE.<sup>21</sup> The inductively coupled plasma (ICP) reactor used for this study, shown in Fig. 1, is patterned after that used by Standaert *et al.*<sup>46</sup> ICP power is supplied through a 3-turn coil sitting on a 1.9 cm thick, 23 cm diameter quartz window at the top of the reactor and the plasma is generated below this window. The process gases

TABLE II. Surface reactions for Cu IMPVD with an Ar buffer gas.

Reaction <sup>a,b</sup>	$p_0$	$E_{th}(eV)$	$E_r(eV)$	$n$	Ref.
$Ar^+ + Cu_s \rightarrow Ar_g + Cu_g$	0.35	45	100	1.0	Eq. (1)
$Ar^+ + SiO_{2s} \rightarrow Ar_g + SiO_{2g}$	0.10	45	100	0.5	Eq. (1)
$Cu^+ + Cu_s \rightarrow Cu_g + Cu_g$	0.35	45	100	1.0	Eq. (1)
$Cu^+ + Cu_s \rightarrow Cu_s + Cu_s$	0.55				
$Cu^+ + Cu_s \rightarrow Cu_g + Cu_s$	0.10				
$Cu^+ + SiO_{2s} \rightarrow Cu_g + SiO_{2g}$	0.10	45	100	0.5	Eq. (1)
$Cu^+ + SiO_{2s} \rightarrow Cu_s + SiO_{2s}$	0.80				
$Cu^+ + SiO_{2s} \rightarrow Cu_s + SiO_{2g}$	0.10				
$Cu_g + Cu_s \rightarrow Cu_s + Cu_s$	0.95				
$Cu_g + SiO_{2s} \rightarrow Cu_s + SiO_{2s}$	0.70				

<sup>a</sup> $s$  refers to surface species and  $g$  refers to gas species. All ions return as a hot neutral. Ions and hot neutrals have the same mechanism.

<sup>b</sup>In reactions with no chemical change, the gas species are reflected from the surface. These reactions are not shown in the table.

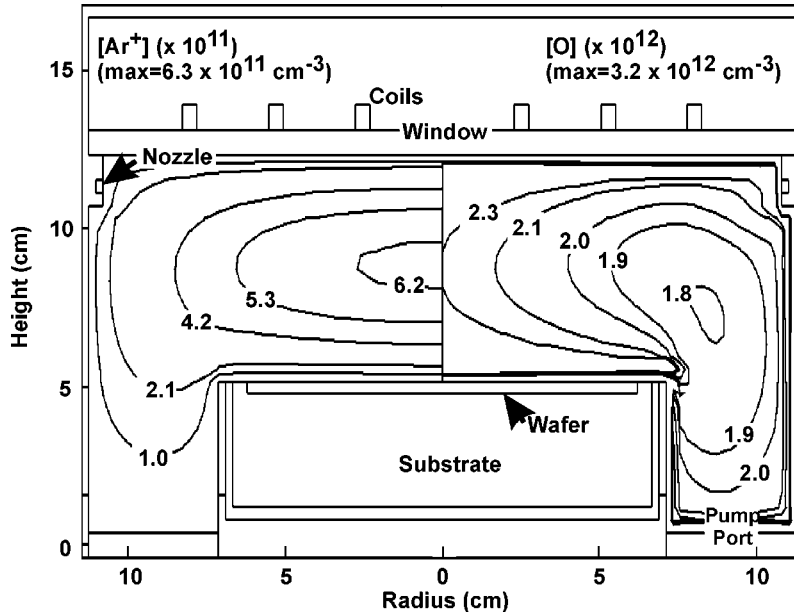


FIG. 1. Plasma properties of an Ar–O<sub>2</sub>=94/6 plasma for the base case (600 W ICP power, 4 mTorr, 40 sccm) and 40 V rf bias at 3.4 MHz. (a) Ar<sup>+</sup> and (b) O atom density. As diffusive transport dominates at low pressures, the ion densities peak near the center.

are injected into the reactor by a nozzle under the quartz window. The gas flow rate (40 sccm), pressure (4 mTorr), and ICP power (600 W at 13.56 MHz) were held constant. The 125 mm wafer is on a substrate 7 cm below the quartz window and was maintained at 10 °C for all simulations. The substrate is independently biased at 3.4 MHz to produce directional ions to the wafer.

Typical densities of Ar<sup>+</sup> and O radicals are shown in Fig. 1. The feed gas is Ar–O<sub>2</sub>=94/6 and the rf bias is 40 V at 3.4 MHz. The power deposition and dominant ionization are confined to 2 to 3 cm below the coils and the transport of electrons and ions are primarily governed by ambipolar diffusion. Hence the Ar<sup>+</sup> density peaks at the center of the reactor. The O radical density is also high near the nozzle as O radicals are the product of electron impact dissociation of the O<sub>2</sub> feed gas.

Fluxes of Ar<sup>+</sup>, O<sub>2</sub><sup>+</sup>, O<sup>+</sup>, and O to the wafer as a function of radius for the same conditions are shown in Fig. 2(a). The dominant ion for these conditions is Ar<sup>+</sup>. Fluxes of Ar<sup>+</sup> and O atoms, which are the key precursors in the etch kinetics, decrease moderately with radius resulting in less activation and lower sputtering at the edge of the wafer. For these conditions etch rates for blanket etching of PTFE at the edge of the wafer were ≈20% lower than at the center. The energy and angular distribution of the Ar<sup>+</sup> flux, shown in Fig. 2(b), has an average energy of ≈75 eV and angular spread of <10°.

Total ion and O fluxes to the center of the wafer for different Ar–O<sub>2</sub> ratios as a function of the applied rf bias are shown in Fig. 3. Increasing the O<sub>2</sub> mole fraction results in a corresponding increase in the flux of O atoms and decrease in the ion fluxes. O radical fluxes are not sensitive to changes in the applied rf bias. However, ion fluxes increase ≈10% when the rf bias is increased to 80 V. Bias power as a function of applied rf bias voltage and gas mixture is shown in Fig. 3(c). With increasing Ar fraction, there is an increase in

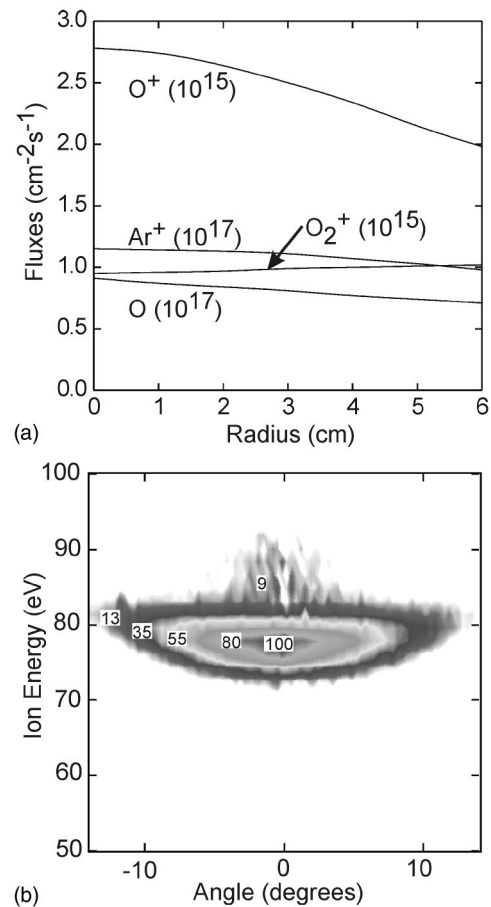


FIG. 2. Properties of the fluxes to the wafer for the base case conditions for Ar–O<sub>2</sub>=94/6 and 40 V bias (a) Ar<sup>+</sup>, O<sub>2</sub><sup>+</sup>, O<sup>+</sup>, and O fluxes as a function of radius. (b) Ar<sup>+</sup> angular and energy distributions incident on and averaged over the wafer.

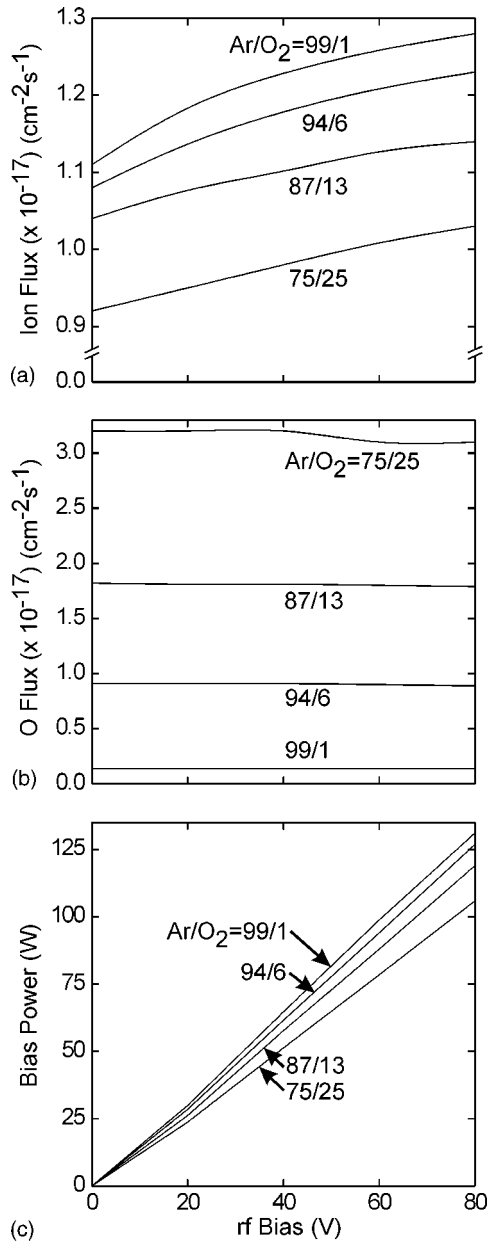


FIG. 3. Plasma properties as a function of gas composition and bias on the wafer for the base case conditions. (a) Ion flux and (b) O atom flux to the center of the wafer; and (c) bias power. Increasing Ar $^+$  flux at higher Ar fractions produce larger currents and bias powers.

the total ion flux to the wafer, which increases current and power deposition for a given rf bias.

Etch rates as a function of bias power for blanket etching of PTFE in Ar–O $_2$  mixtures are shown and compared to experiments in Fig. 4.<sup>21</sup> For a given gas mixture, the O atom flux is nearly independent of bias power, and so the rate of formation of activated polymer sites is constant. The increase in etch rates with increasing bias power is attributed to an increase in the sputtering of activated polymer sites which releases volatile etch products such as CO $_x$ , COF $_x$ , and F $_2$ . At low biases increases in the etch rates with increasing O $_2$  are small which indicate that the sputtering of activated sites is the rate-limiting step. In contrast, at 100 W bias

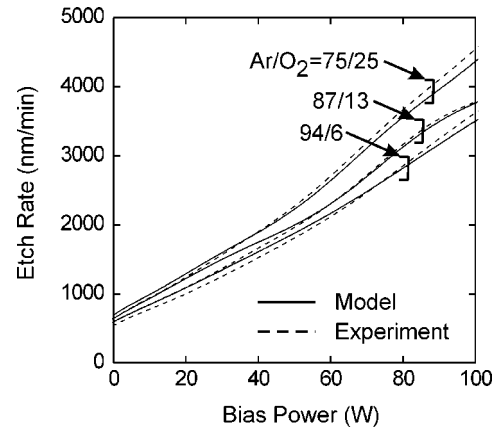


FIG. 4. A comparison of predicted and experimental results for PTFE etch rates as a function of bias power for Ar–O $_2$  chemistries. Etch rates increase with bias power. Experimental results are from Ref. 21.

power, increasing the O $_2$  from 6% to 25% increases etch rates from 3500 to 4500 nm/min. At these bias powers oxidation of the polymer surface to form activated sites is the rate-limiting step. These results are also consistent with earlier observations that oxygen plasma etching of organic polymer has distinct oxygen-neutral limited and ion-limited regimes.<sup>19</sup>

## B. Sensitivity of the mechanism

The sensitivity of polymer etch rates on coefficients describing formation [Eq. (8)] and sputtering of activated sites [Eq. (9)] was investigated. For example, etch rates as a function of O atom sticking probability to form activated sites for the base case conditions and Ar–O $_2$ =75/25 are shown in Fig. 5. Without a bias, etching is limited by the sputtering rates. As a result increasing  $p_0$  has little effect on etching. As the substrate bias increases, ion energies increase sufficiently to sputter activated sites thereby exposing more polymer surface to further oxidation. As a result, etch rates increase with  $p_0$  at intermediate biases. However, further increasing the bias increases the rate of direct sputtering of non-activated sites by ions which then becomes the dominant polymer removal process. Hence the variation of etch rate as a function of  $p_0$  is small at large biases. Based on these observations, similar parameterizations for other gas mixtures and comparisons to experiments, we chose  $p_0=0.50$ .

The sensitivity of sputtering of activated polymer sites was also investigated for the same process conditions. The resulting etch rates are also shown in Fig. 5. Since at low rf bias, the ion sputtering is rate limiting, decreasing  $E_t$  significantly increases the fraction of ions that are able to sputter activated sites. Without an applied bias (ions arriving at the substrate with energies corresponding to the floating potential) etch rates increased to 2000 nm/min when  $E_t$  is decreased from 15 eV. High biases produce etching in the neutral-limited regime and as a result changes in  $E_t$  have little effect on the etch rates. Increasing  $p_0$  increases etch

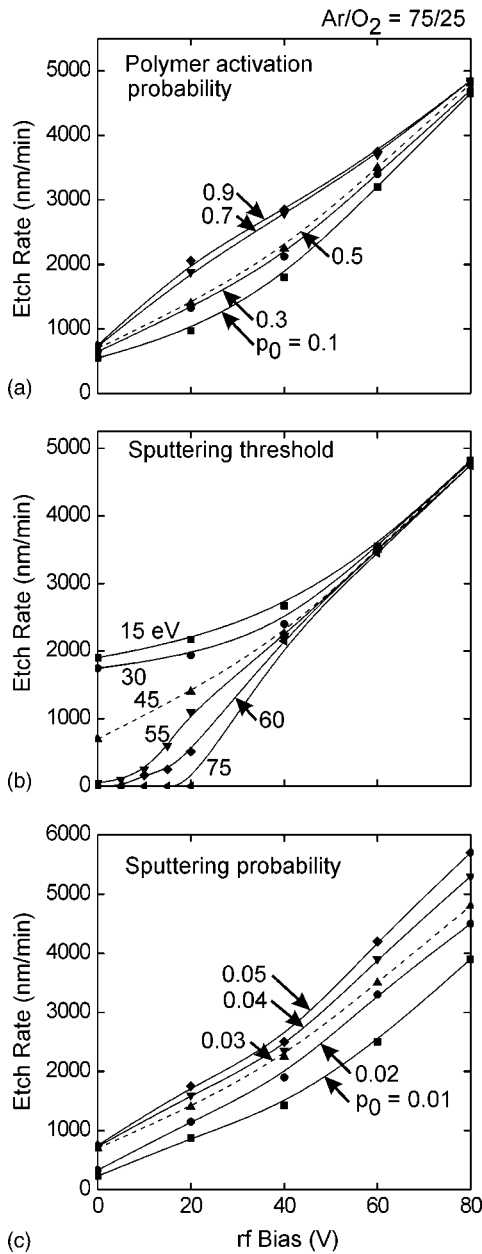


FIG. 5. Consequences of varying parameters in the reaction mechanism for the base case conditions and Ar-O<sub>2</sub>=75/25 as a function of rf bias. (a) Probability of formation of activated polymer site; (b) threshold energy of the sputtering of an activated polymer site; and (c) sputtering probability of the activated polymer site. At low biases, the dominant polymer removal process is sputtering of activated sites. At high biases, polymer is removed by direct sputtering.

rates for all substrate biases. Based on these parameterizations and comparison to experiments we chose  $E_t=45$  eV and  $p_0=0.03$ .

## V. STRIPPING OF RESIDUAL FLUOROCARBON POLYMER

Stripping of residual polymer from vias and trenches of SiO<sub>2</sub> etched in fluorocarbon plasmas has become increasingly challenging with the reduction in feature sizes and increase in the aspect ratio of the features. Use of O<sub>2</sub> plasmas

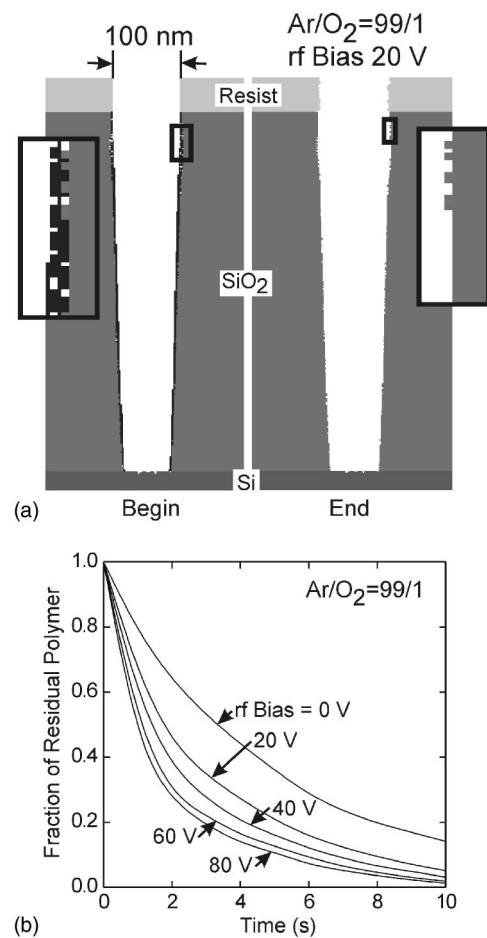


FIG. 6. Polymer stripping from SS trenches. (a) Profiles of the SS trench before and after the cleaning process using Ar-O<sub>2</sub>=99/1, 20 V rf bias and the base case conditions. The aspect ratio is 5 and the trench opening is 100 nm. The black material is polymer. Expanded views of selected outlined portions of the profile are shown in the adjacent boxes. (b) Stripping efficiency as a function of rf bias. As in blanket etching of PTFE, stripping is more efficient at higher biases due to higher rates of sputtering of activated polymer sites.

for this purpose, although common practice for SS films, has yet to be optimized for PS films due to their complex pore morphologies and their more complex interactions with the plasma species.

## A. Stripping polymer from solid SiO<sub>2</sub> trenches

The ICP reactor that was used for the etching of the SS and PS trenches is the same as that used for the stripping applications. Profiles of high aspect ratio SS trenches before and after stripping are shown in Fig. 6. The etching process conditions were 1400 W ICP power at 13.56 MHz, 6 mTorr pressure, 40 sccm CHF<sub>3</sub> flow rate and a self generated dc bias of -65 V. These process conditions were optimized to obtain a profile with nearly vertical sidewalls. The aspect ratio of the profile is 5 with a trench opening of 100 nm. (These are the dimensions for all trenches discussed here.) The taper of the profile calculated as the ratio of the width of the trench at 400 nm from the bottom to the width at the top of the trench is 0.98. The stripping process conditions are the

base case with  $\text{Ar-O}_2=99/1$  and rf bias=20 V. The post etch residual polymer thickness on the sidewalls for this case is  $\approx 5$  nm and on the bottom of the trench is a few monolayers. This difference is a result of there being less ion sputtering of the passivation layer on the sidewalls of the profiles during etching due to the high degree of anisotropy of ions. In contrast the directional ions are more efficient in delivering activation energy to the bottom of the trench and hence reduce the thickness of the polymer there. These process conditions nearly completely remove polymer from the SS trench. Note that there is surface roughness on the sidewalls of the trenches. The implications of this roughness will be discussed below.

Stripping efficiency (the fraction of polymer remaining) for the same conditions using  $\text{Ar-O}_2=99/1$  while varying the substrate bias is shown in Fig. 6(b) as a function of time. As in blanket etching, at low biases there are low rates of sputtering of activated polymer sites and the ion activated process removal process is the rate limiting step resulting in poor stripping. As the bias increases there is increased removal of polymer due to both chemically enhanced and direct sputtering. Note that the cleaning times are short as only 5–10 nm of material need to be removed from the sidewalls. These times are short compared to those required to remove the much thicker photoresist.

## B. Stripping polymer from porous $\text{SiO}_2$ trenches

The stripping of residual fluorocarbon from trenches in PS having closed pores and 50% porosity and different average pore radii is shown in Fig. 7. The process conditions are the base case,  $\text{Ar-O}_2=99/1$  and a rf bias of 20 V at 3.4 MHz. Results are shown for a time corresponding to removing 99% of the polymer for the 4 nm pore case. Profiles are also shown before and after stripping. Note the filling of pores by polymer, particularly with the larger pores. The pore filling results from initial activation by low energy ions or reflected neutrals, species which can arrive at the surface with a broad angular spread.

Stripping efficiencies generally decrease with increasing average pore radius. The nonmonotonic change in efficiency (at a given time) between, for example, 10 and 13 nm pore cases results from the stochastic nature of the pore morphology and resulting random nature of view angles to the plasma. When PS with 4 nm pores is 99% cleaned of polymer nearly 24% of the residual polymer remains for the 16 nm case. The cleaning is more effective at the top of the trench than the bottom of the trench due to the lack of favorable view angles for the incident ions at the lower location. This is particularly so for the inner surfaces of pores where significant polymer remains. These locations at best receive hot neutrals from ion reflection which have lower energies than the incident ions. This results in poor ion sputtering and removal of the polymer. On the other hand, the formation of polymer at these sites during fluorocarbon etching results from neutral flux and low ion energy activation. The neutral and low energy ion (or reflected neutral) fluxes being more

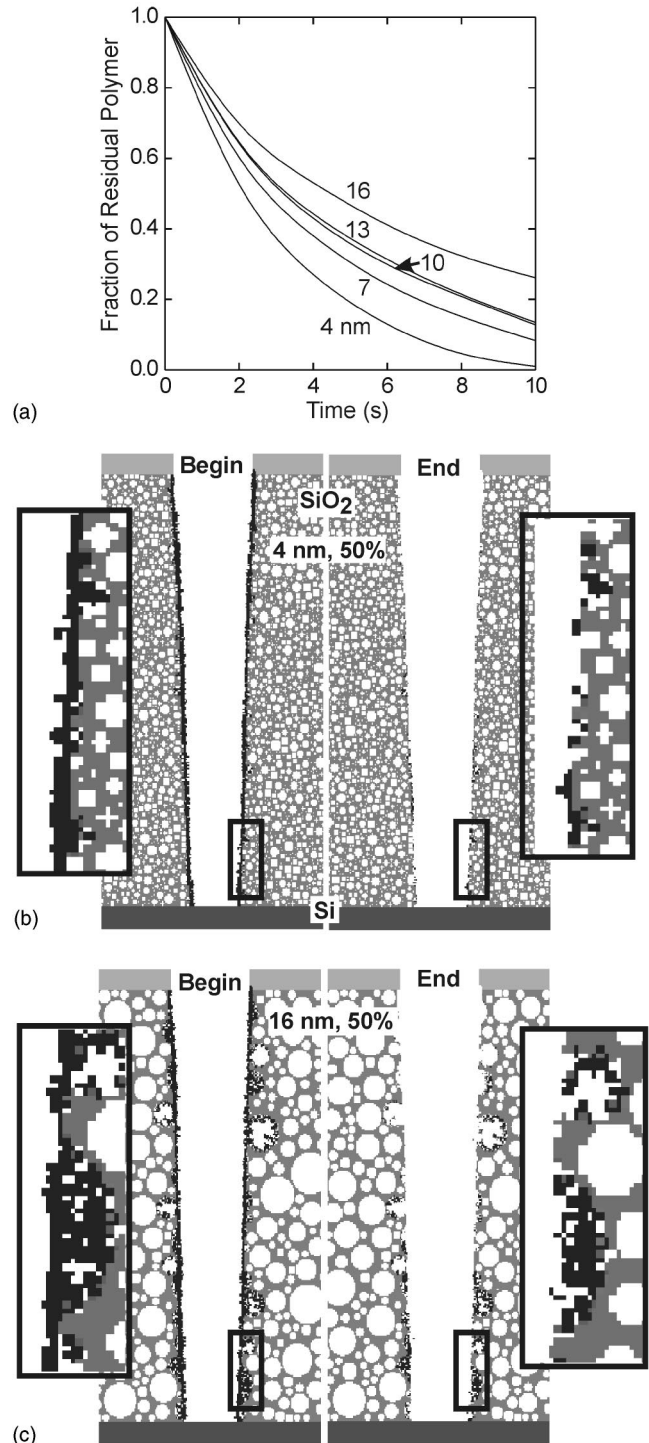


FIG. 7. Polymer stripping from PS trenches. (a) Stripping efficiency as a function of time for PS with closed pores, 50% porosity and different average pore radii. The process conditions are the base case with  $\text{Ar-O}_2=99/1$  and a 20 V rf bias. Profiles of the trenches are shown before and after stripping for PS with (b)  $r_0=4$  nm and (c)  $r_0=16$  nm. The black material is polymer. Expanded views of selected outlined portions of the profile are shown in the adjacent boxes. Unfavorable view angles due with larger pores leads to inefficient stripping.

isotropic in nature are less sensitive to the pore morphology and so polymer is able to be deposited on all surfaces of the pores.

The inefficiencies in stripping due to the complex pore

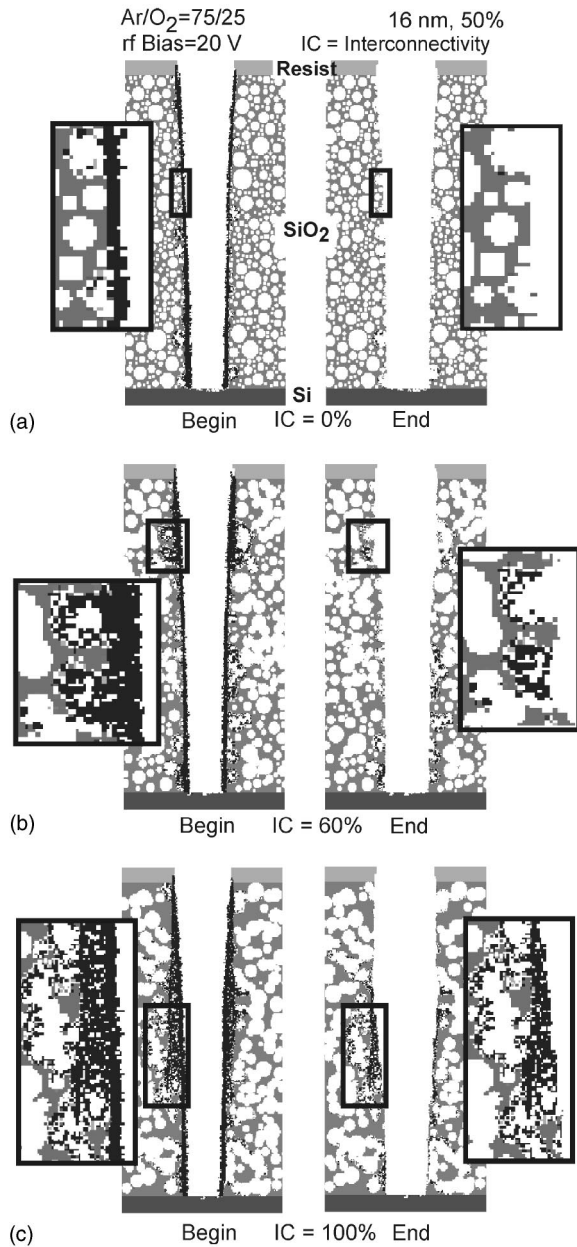


FIG. 8. Profiles before and after stripping using an Ar–O<sub>2</sub>=75/25 plasma for the base case with a 20 V rf bias. The PS has 16 nm pores and 50% porosity. Results are shown for interconnectivities of (a) 0%, isolated pores, (b) 60% and (c) 100%. The black material is polymer. Expanded views of selected outlined portions of the profile are shown in the adjacent boxes. Stripping becomes less efficient with large interconnectivities.

morphology which occur in a closed pore network are magnified by interconnected networks. For example, profiles of high aspect ratio trenches in interconnected PS films before and after cleaning using an Ar–O<sub>2</sub>=75/25 plasma for the base case conditions and rf bias of 20 V are shown in Fig. 8. The cleaning time is 10 s (same scale as for Fig. 7) which removes 99% of the polymer from a 4 nm closed pore network in an Ar–O<sub>2</sub>=99/1 plasma. View angles for ions or reflected neutrals inside the interconnected chains become even more unfavorable and so the activated polymer surface sites inside the chains are less likely to receive particle fluxes

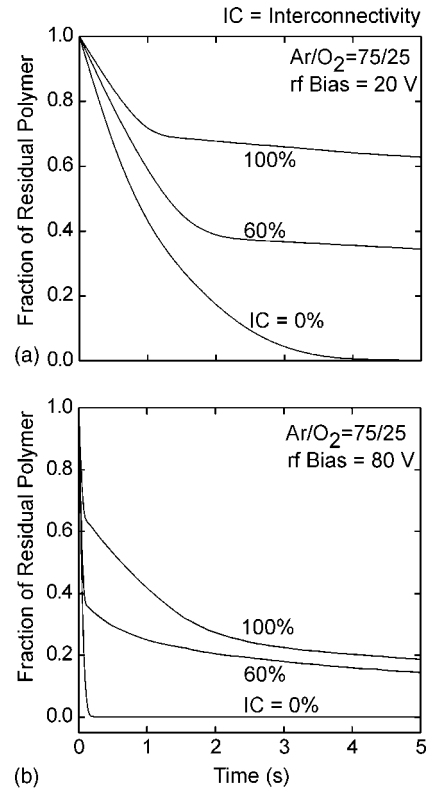


FIG. 9. Effect of interconnectivity and bias on the fraction of residual polymer remaining on PS using an Ar–O<sub>2</sub>=75/25 plasma for the base case with (a) 20 V rf bias and (b) 80 V rf bias. The PS has  $r_0 = 16$  nm.

with sufficient energies to remove material. The end result is that residual polymer remains deep within the interconnected pores. With interconnected structures there is also the likelihood for O radicals to penetrate into the porous network which could change the dielectric properties of the film by reacting with organic groups.

The stripping efficiencies of residual fluorocarbon from PS with a pore size of 16 nm (50% porosity) as a function of time for different interconnectivities are shown in Fig. 9. The process conditions are Ar–O<sub>2</sub>=75/25 and substrate rf biases of 20 and 80 V. With a closed pore network, increasing the substrate bias compensates for unfavorable view angles by increasing the energy of reflected neutrals into open pores and produces nearly complete polymer removal. In contrast, a 20 V bias leaves 0.63 and 0.35 of the polymer in the 60% and 100% interconnected samples as energetic particles are unable to penetrate sufficiently deep into the network to activate removal. Increasing the bias to 80 V reduces the residual polymer fraction to 0.2 for a 100% interconnected structure as particles even after a few reflections still have sufficient energy to sputter the activated polymer. Even higher substrate biases would be required to deliver the required energy inside the pore chains for complete cleaning of the residues, though there may be locations from which the polymer cannot be removed due to statistically poor view angles. The downside to this increase in bias is sputtering damage to the PS film.

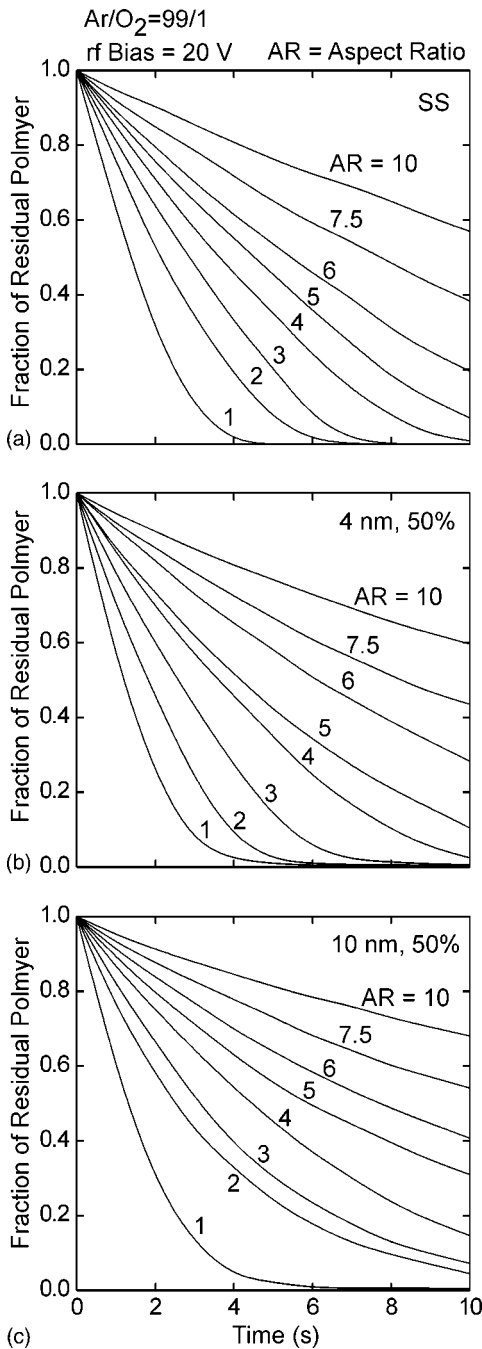


FIG. 10. Effect of aspect ratio on stripping efficiencies for trenches cleaned using an Ar–O<sub>2</sub> = 99/1 plasma for the base case with 20 V rf bias. (a) SS, (b) PS with  $r_0 = 4$  nm and 50% porosity and (c)  $r_0 = 10$  nm, 50% porosity.

### C. Consequences of aspect ratio

Stripping was investigated for SS and PS trenches having different aspect ratios. These stripping efficiencies are shown in Fig. 10 for an Ar–O<sub>2</sub> = 99/1 and rf bias = 20 V. Profiles for the 16 nm case for aspect ratios of 1, 3, and 5 are shown in Fig. 11. The time for cleaning was chosen so that 99% of the polymer was removed for SS trenches with an aspect ratio of 4. The general trend is more rapid polymer removal for lower AR features. For a given aspect ratio, cleaning is less rapid as pore sizes increases. The scaling with aspect

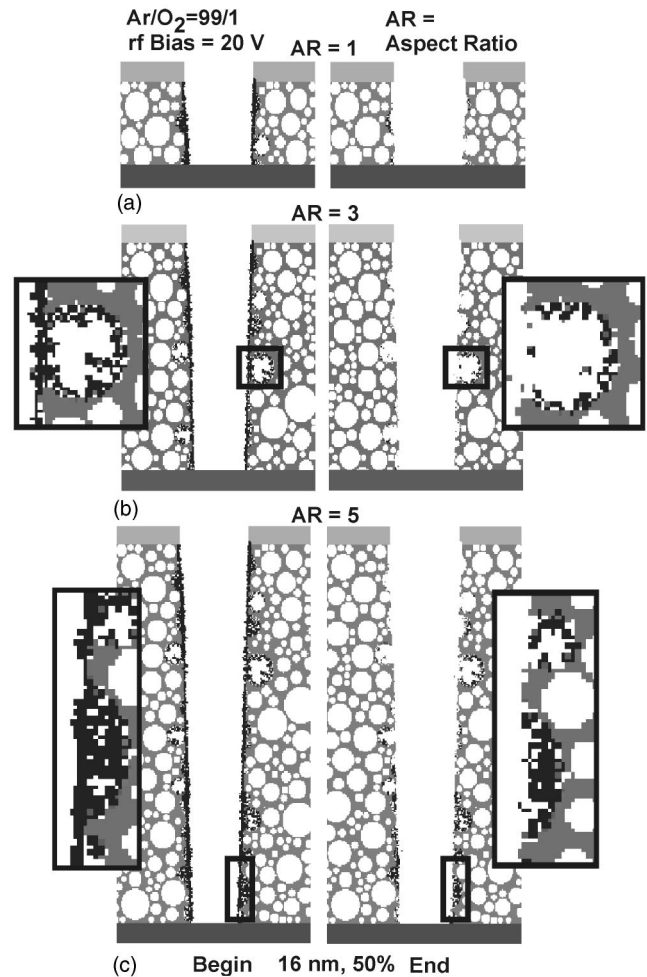


FIG. 11. Profiles of PS trenches with  $r_0 = 16$  nm and 50% porosity cleaned using an Ar–O<sub>2</sub> = 99/1 plasma for the base case with 20 V rf bias for different aspect ratios (a) AR = 1, (b) 3, and (c) AR = 5. The black material is polymer. Expanded views of selected outlined portions of the profile are shown in the adjacent boxes. Better view angles to the ion flux at the top and reflected ions the bottom of the trench improve stripping for low and intermediate aspect ratios.

ratio is in part due to being in a reactant limited regime. The magnitude of the reactant current into the trench is determined by the width of the trench. As the aspect ratio increases a larger surface area must be cleaned by a constant current of reactants. The exposed surface area increases as the porosity increases. On this basis alone the cleaning time should increase in proportion to the fractional increase in surface area. Additional increases in cleaning time beyond the ratio of surface area are due to nonlinear processes.

For low aspect ratio trenches the pore morphology has little effect on the cleaning times. The views angle to the plasma from all surfaces is sufficiently large, or the shadowing sufficiently small, that energetic particles (direct or reflected) can reach into pores to sputter polymer. Having said that, polymer stripping also depends on the location in the trench. For example, for trenches with an aspect ratio of 3, pores near the top of the trench have large view angles to ions and so are left with little residual fluorocarbon. Pores at the bottom of the trench also have little residual fluorocarbon

as they receive energetic particles resulting from ions reflecting from the bottom of the trench. Pores located in the middle of the trench see fewer ions impacting directly or following reflection and so considerable residual polymer is left. For example, the overall cleaning efficiency for the feature having an aspect ratio of 3 is  $\approx 10\%$  and which is mostly attributable to this middle region. For an aspect ratio of 5, the cleaning efficiencies for top 100 nm, middle 300 nm, and bottom 100 nm of the trench are 3%, 30%, and 40%, respectively. The overall cleaning efficiency in this case is 33%. As the aspect ratio increases, the view angles at the bottom of the trench decrease and the ions reflected from the bottom of the trench contribute less towards the stripping process.

## VI. BARRIER COATINGS BY IMPVD

### A. Reactor scale properties and coating solid $\text{SiO}_2$

Barrier coatings and seed layers of metals are typically deposited by PVD or IMPVD. Although Cu is not used for barrier coatings, we are using Cu IMPVD as a surrogate for these studies as the knowledge base for that system is well established. The IMPVD reactor used for this study, schematically shown in Fig. 12, has been extensively discussed earlier and so is briefly described here.<sup>47</sup> The reactor has a conventional dc magnetron copper target augmented by internal inductively coupled coils which provide auxiliary ionization. The diameters of the target and of the substrate are 20 cm. The distance between the target and the substrate is 13 cm. The process conditions are 1000 W ICP power, 300 W magnetron power, 40 mTorr Ar gas buffer and 150 sccm gas flow rate. The magnetic field is 250 G at the surface of the target. The rf voltage on the inductive coil is 100 V and the self generated dc bias is  $-90$  V. The rf and dc bias combination results in about 20 V of rf oscillation in the plasma potential.

Fluxes of selected radicals and neutrals incident onto the wafer are shown in Fig. 12(b). Due to a high pressure of 40 mTorr which slows sputtered Cu and so allows them to be ionized, the majority of the incident Cu flux is  $\text{Cu}^+$ . The majority of the neutral Cu flux to the wafer consists of (metastable)  $\text{Cu}^*$ .  $\text{Cu}^+$  has an ion energy distribution between 40 and 80 eV, which is primarily due to the oscillation in the plasma potential from the immersed coil.  $\text{Cu}^+$  flux is dominantly anisotropic and has an angular spread of  $\pm 15^\circ$  from the normal. In contrast the  $\text{Cu}^*$  has energies between 0.1 and 0.7 eV and an isotropic angular distribution.

Barrier layers for an initially smooth ideal SS trench, and a SS trench etched in a fluorocarbon plasma and stripped using an oxygen plasma are shown in Fig. 12 as well. When the SS surface is initially smooth, the resulting film is conformal with similar sidewall and bottom coverage, as shown in Fig. 12(c). Even in this case there is some small amount of roughness in the final Cu barrier layer due to sputtering of the  $\text{SiO}_2$  sidewalls and Si bottom layer during the IMPVD process. This surface roughness is then magnified by shadowing during the deposition process which has a directional component. When the initial surface has roughness, as in Fig.

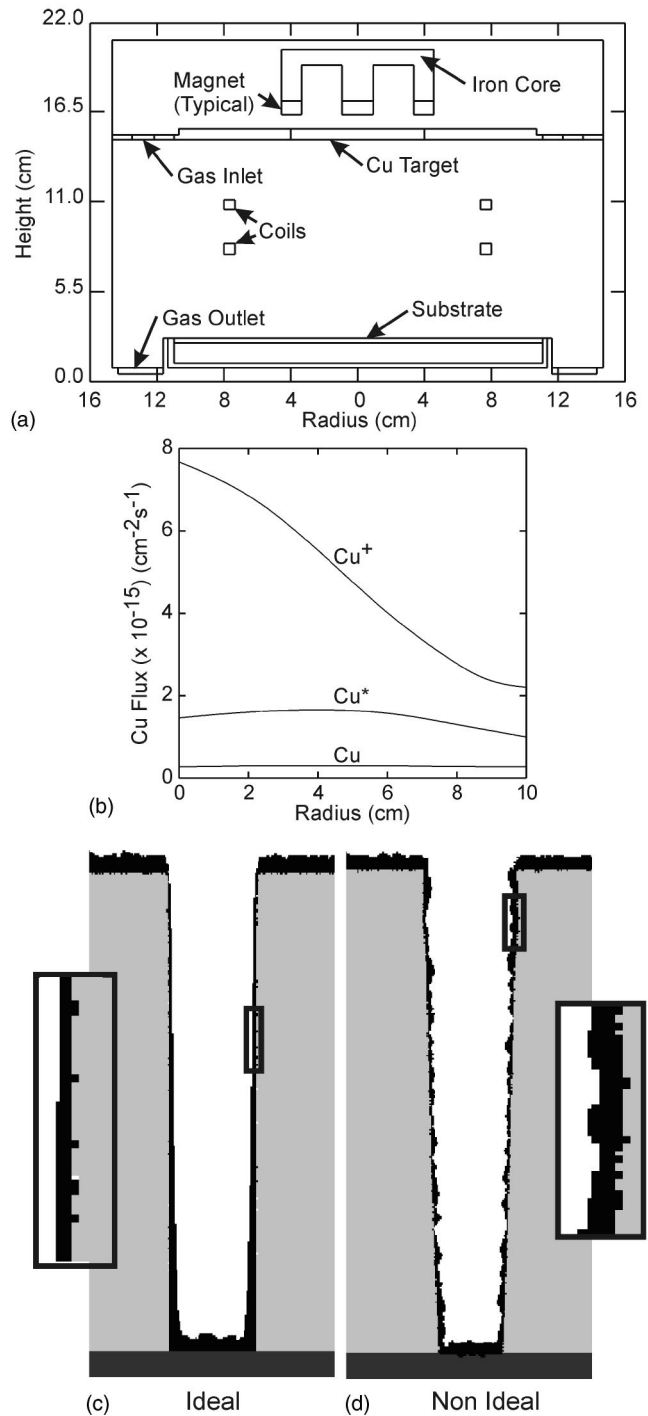


FIG. 12. Cu IMPVD as a surrogate for barrier coatings. (a) Schematic of the IMPVD reactor, (b) Fluxes of  $\text{Cu}^+$ ,  $\text{Cu}^*$ , and Cu to the wafer for the base case. Profiles of SS trenches coated using Cu IMPVD for (c) a smooth ideal trench and (d) a trench obtained after etching and stripping. The black material is copper. Expanded views of selected outlined portions of the profile are shown in the adjacent boxes. Sputtering during prior processing steps results in sidewall roughness, which by micro shadowing produces unevenness in the deposited film.

12(d), the resulting film has significant thickness variation. The initial roughness here results from sputtering during the etch and cleaning processes and is magnified by the finite size of our numerical mesh. Nevertheless it is illustrative of

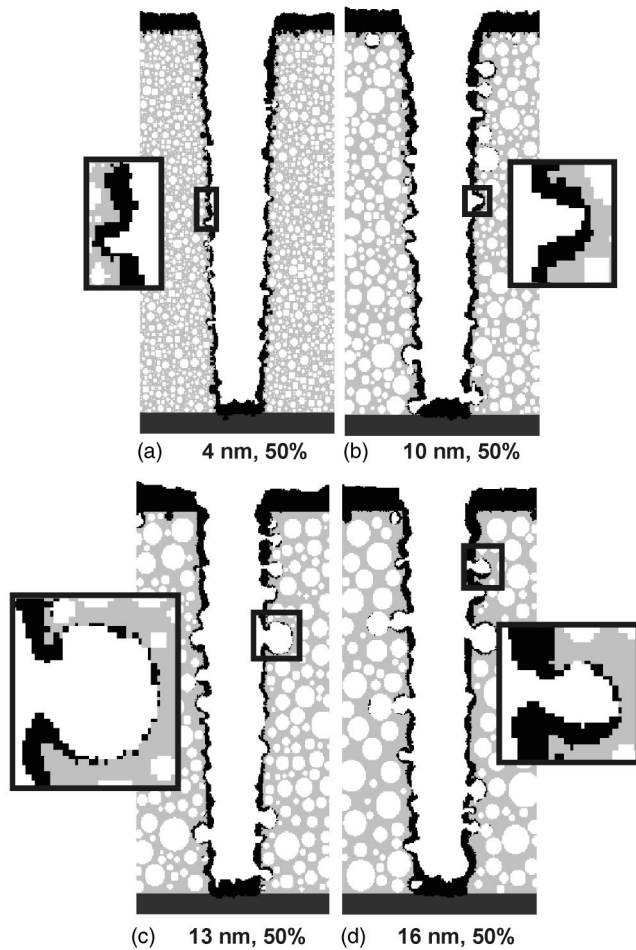


FIG. 13. Cu IMPVD onto PS trenches with 50% porosity for different average pore radii. (a) 4 nm, (b) 10 nm, (c) 13 nm, and (d) 16 nm. The black material is copper. Expanded views of selected outlined portions of the profile are shown in the adjacent boxes. The film is less conformal for larger pores and voids are created or initiated due to the presence of pores.

the consequences of sidewall roughness, which by micro shadowing produces unevenness in the film. The direct result is that thicker films are required to ensure that no pinholes or critically thin regions occur.

### B. Scaling of coating porous $\text{SiO}_2$

This need for thicker average films to mask roughness extends to PS. Barrier layers for closed PS (4, 10, 13, and 16 nm at 50% porosity) are shown in Fig. 13. The process conditions were optimized to achieve a conformal coating for SS, which is shown in Fig. 12(d). The deposition times are different for each pore size to achieve similar sidewall thickness of  $\approx 3\text{--}5$  nm. For 4 nm PS, the ratio of the film thickness on the top of the feature to the sidewalls ( $R$ ) required to obtain conformal coverage is  $R \approx 3$ , while that for SS is  $R \approx 2$ . This value increases to  $R \approx 6$  for the 10 nm PS. For 13 and 16 nm PS conformal coverage could not be achieved even when  $R > 6$ . In this case the pores are large enough that the species fluxes are inefficient in tracing the complex pore morphology and producing conformal coverage. The alterna-

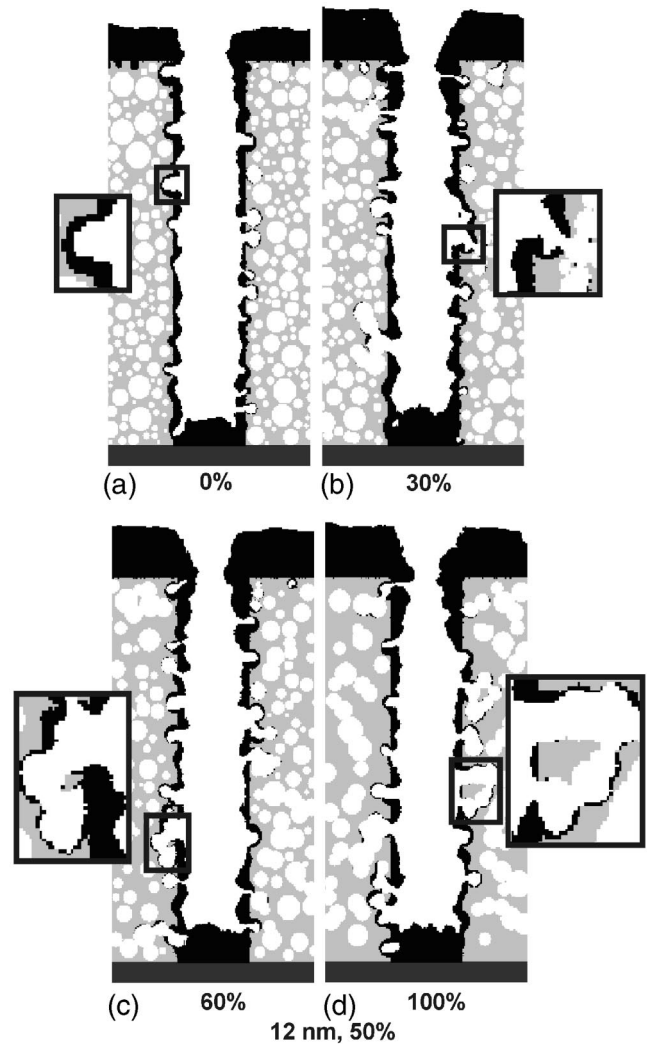


FIG. 14. Effect of interconnectivity on Cu IMPVD into PS trenches with  $r_0 = 12$  nm and 50% porosity for different interconnectivities. (a) 0%, (b) 30%, (c) 60%, and (d) 100%. The black material is copper. Expanded views of selected outlined portions of the profile are shown in the adjacent boxes. Thicker coatings are required for pore sealing and to avoid pin-hole formation. Thicker coating also leads to narrowing of the trench opening and pinch-off.

tive would be to bridge the gap at the pore openings, which would require barrier coating thickness of at least the pore diameter.

Similar challenges are faced when depositing barrier layers into PS trenches having interconnected networks. In these cases, the goal is to seal the opening to the interconnected chains with the diffusion barrier. Conformal coating of the barrier layer onto the surface of isolated pores produces an adequate diffusion barrier. However for interconnected pores it is likely not possible for the depositing species to map onto the contours of the chains deep into the PS to produce a conformal coating. As a result, sealing of the opening of the pore chain is required.

To investigate the efficiency of depositing barrier coatings onto interconnected pores, Cu IMPVD onto PS trenches (4 and 12 nm with 50% porosity) for varying degrees of inter-

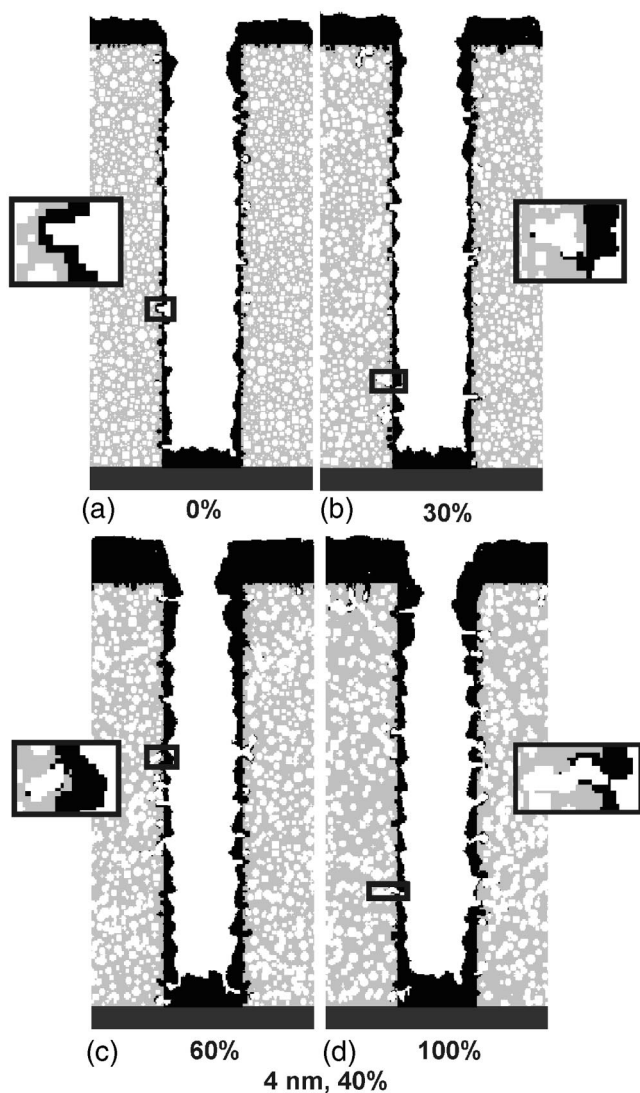


FIG. 15. Effect of interconnectivity on Cu IMPVD into PS trenches with  $r_0=4$  nm and 40% porosity for different interconnectivities. (a) 0%, (b) 30%, (c) 60%, and (d) 100%. The black material is copper. Expanded views of selected outlined portions of the profile are shown in the adjacent boxes. Sealing of the chains by the barrier layer is more efficient for small pores.

connectivity was modeled. The resulting profiles are shown in Figs. 14 and 15. To bridge the chain openings, a coating thickness on the sidewalls of at least the average pore diameter is required. As the desired film thickness is 5–8 nm, this becomes problematic for larger pores and larger porosities. As the deposition time increases to provide the thicker sidewall films, the buildup of film at the top of the trench narrows the trench opening. This reduces the view angles of the plasma from inside the trench and further decreases the efficiency of deposition. Eventually this buildup of film at the top of the trench could lead to pinch-off. In these instances, process conditions would need to be re-optimized to sputter away metal accumulating at the lips of the trench.

Networks with small interconnectivities ( $\leq 30\%$ ) and small pores, 4 nm in this example, are able to be sealed with  $R \approx 4-6$ . Larger interconnectivities have unabridged pores

with similar film thicknesses, an artifact of the pore size distribution and orientation of the networks. Statistically larger pores with vertically oriented chains present a larger opening at the surface of the trench which must then be sealed. In this regard, it was at best problematic to seal 4 nm chains with 60% interconnectivity. Sealing the 12 nm PS was at best problematic for even small interconnectivities as exposed chains can statically present 15–20 nm openings. In some cases, conformal deposition in the larger pores at low interconnectivities effectively seals the network. This opportunity is statistically lost for larger interconnectivities.

## VII. CONCLUDING REMARKS

Plasma etching of trenches in PS and SS using fluorocarbon plasmas leaves a residual polymer film. Stripping of the fluorocarbon polymer was investigated using a surface reaction mechanism developed for organic polymers etched in Ar–O<sub>2</sub> chemistries. This mechanism was incorporated into a feature scale model coupled to a reactor scale model. Etching of fluorocarbon polymer was modeled as being activated by O atoms and chemically sputtered by energetic ions. Stripping efficiencies were higher in SS than PS and decreased for higher aspect ratio features. Stripping was less efficient in PS having large pores due to unfavorable view angles into pores for the incoming ion fluxes. These unfavorable view angles resulted in cleaning being less effective for interconnected PS in which polymer may be deposited deep into the network. Since deposition of polymer is activated by low energy ions (or reflected neutrals) but removal requires high energy particles, polymer can be deposited in recesses from which it is difficult to clean. Cu IMPVD was investigated as a surrogate to barrier coating and seed layer deposition into PS trenches. Deposition can be conformal for PS with small pores but for pores  $>10$  nm, obtaining conformal coatings is problematic. With interconnected PS the goal is to seal openings to the network and so thicker films are required for larger pores and higher connectivities. These thicker films may lead to pinch-off during the deposition process.

## ACKNOWLEDGMENTS

This work was supported by the National Science Foundation (CTS99-74962, CTS03-15353), Semiconductor Research Corporation and Sematech.

- <sup>1</sup>S.-J. Wang, H.-H. Park, and G.-Y. Yeom, *Jpn. J. Appl. Phys., Part I* **39**, 7007 (2000).
- <sup>2</sup>K. Maex, M. R. Baklanov, D. Shamiryan, F. Iacopi, S. H. Brongersma, and Z. S. Yanovitskaya, *J. Appl. Phys.* **93**, 8793 (2003).
- <sup>3</sup>S. J. Fonash, *J. Electrochem. Soc.* **137**, 3885 (1990).
- <sup>4</sup>G. S. Oehrlein, T. E. F. M. Standaert, and P. J. Matsuo, in *Solid State Technology; Vol. May 2000* (2000), p. 125.
- <sup>5</sup>H. Seo, S. B. Kim, J. Song, Y. Kim, H. Soh, Y. C. Kim, and H. Jeon, *J. Vac. Sci. Technol. B* **20**, 1548 (2002).
- <sup>6</sup>K. Ueno, V. M. Donnelly, and Y. Tsuchiya, *J. Vac. Sci. Technol. B* **16**, 2986 (1998).
- <sup>7</sup>D. Shamiryan, M. R. Baklanov, S. Vanhaelemeersch, and K. Maex, *J. Vac. Sci. Technol. B* **20**, 1923 (2002).

- <sup>8</sup>N. R. Rueger, J. J. Beulens, M. Schaepkens, M. F. Doemling, J. M. Mirza, T. E. F. M. Standaert, and G. S. Oehrlein, *J. Vac. Sci. Technol. A* **15**, 1881 (1997).
- <sup>9</sup>M. Schaepkens, G. S. Oehrlein, C. Hedlund, L. B. Jonsson, and H. O. Blom, *J. Vac. Sci. Technol. A* **16**, 3281 (1998).
- <sup>10</sup>Y. Wang, S. W. Graham, L. Chan, and S. Loong, *J. Electrochem. Soc.* **144**, 1522 (1997).
- <sup>11</sup>G. S. Oehrlein, G. J. Scilla, and S. Jeng, *Appl. Phys. Lett.* **52**, 907 (1988).
- <sup>12</sup>D. K. Schroder, *Semiconductor Material and Device Characterization* (Wiley, New York, 1990).
- <sup>13</sup>S. D. Gendt, P. Snee, I. Cornelissen, M. Lux, R. Vos, P. W. Mertens, D. M. Knotter, and M. M. Heyns, *Symp. VLSI Technol. Dig. Tech. Papers*, 168 (1998).
- <sup>14</sup>H. Ying, J. P. Barnak, Y. L. Chen, and R. J. Nemanich, *Mater. Res. Soc. Symp. Proc.* **386**, 285 (1995).
- <sup>15</sup>A. Somashekhar, H. Ying, P. B. Smith, D. B. Aldrich, and R. J. Nemanich, *J. Electrochem. Soc.* **146**, 2318 (1999).
- <sup>16</sup>D. Louis, E. Lajoinie, F. Pires, W. M. Lee, and D. Holmes, *Microelectron. Eng.* **41/42**, 415 (1998).
- <sup>17</sup>F. Greer, J. W. Coburn, and D. B. Graves, *J. Vac. Sci. Technol. A* **18**, 2288 (2000).
- <sup>18</sup>C.-Y. Sin, B.-H. Chen, W. L. Loh, J. Yu, P. Yelehanka, A. See, and L. Chan, *J. Vac. Sci. Technol. B* **20**, 1974 (2002).
- <sup>19</sup>F. Greer, L. Van, D. Fraser, J. W. Coburn, and D. B. Graves, *J. Vac. Sci. Technol. B* **20**, 1901 (2002).
- <sup>20</sup>D. Fuard, O. Joubert, L. Vallier, and M. Bonvalot, *J. Vac. Sci. Technol. B* **19**, 447 (2001).
- <sup>21</sup>T. E. F. M. Standaert, P. J. Matsuo, X. Li, G. S. Oehrlein, T. M. Lu, R. Gutmann, C. T. Rosenmayer, J. W. Bartz, J. G. Langan, and W. R. Entley, *J. Vac. Sci. Technol. A* **19**, 435 (2001).
- <sup>22</sup>H. Cerva, E. G. Mohr, and J. Oppolzer, *J. Vac. Sci. Technol. B* **5**, 590 (1992).
- <sup>23</sup>J. A. Cunningham, *Semicond. Int.* **23**, 97 (2000).
- <sup>24</sup>E. J. O'Sullivan, A. G. Schrott, M. Paunovic, C. J. Sambucetti, J. R. Marino, P. J. Bailey, S. Kaja, and K. W. Semkow, *IBM J. Res. Dev.* **42**, 607 (1998).
- <sup>25</sup>F. Iacopi, Z. Tokei, M. Stucchi, S. H. Brongersma, D. Vanhaeren, and K. Maex, *Microelectron. Eng.* **65**, 123 (2003).
- <sup>26</sup>W. Besling, A. Satta, J. Schuhmacher, T. Abell, V. Sutcliffe, A. M. Hoyas, G. Beyer, D. Gravesteijn, and K. Maex, *Proc. IITC*, 288 (2002).
- <sup>27</sup>F. Iacopi, Z. Tokei, M. Stucchi, F. Lanckmans, and K. Maex, *IEEE Electron. Device Lett.* **24**, 147 (2003).
- <sup>28</sup>R. J. Hoekstra, M. J. Grapperhaus, and M. J. Kushner, *J. Vac. Sci. Technol. A* **15**, 1913 (1997).
- <sup>29</sup>R. J. Hoekstra and M. J. Kushner, *J. Vac. Sci. Technol. B* **16**, 2102 (1998).
- <sup>30</sup>A. Sankaran and M. J. Kushner, *J. Vac. Sci. Technol. A* **22**, 1242 (2004).
- <sup>31</sup>J. Lu and M. J. Kushner, *J. Vac. Sci. Technol. A* **19**, 2652 (2001).
- <sup>32</sup>R. L. Kinder and M. J. Kushner, *J. Appl. Phys.* **90**, 3699 (2001).
- <sup>33</sup>R. L. Kinder and M. J. Kushner, *J. Vac. Sci. Technol. A* **19**, 76 (2001).
- <sup>34</sup>A. M. Barklund and H.-O. Blum, *J. Vac. Sci. Technol. A* **10**, 1212 (1992).
- <sup>35</sup>M. Schaepkens, G. S. Oehrlein, C. Hedlund, L. B. Jonsson, and H.-O. Blum, *J. Vac. Sci. Technol. A* **16**, 3281 (1998).
- <sup>36</sup>C. Steinbruechel, B. J. Curtis, H. W. Lehmann, and R. Widmer, *IEEE Trans. Plasma Sci.* **14**, 137 (1986).
- <sup>37</sup>E. J. H. Collart, J. A. G. Baggerman, and R. J. Visser, *J. Appl. Phys.* **78**, 47 (1995).
- <sup>38</sup>J. A. G. Baggerman, R. J. Visser, and E. J. H. Collart, *J. Appl. Phys.* **75**, 758 (1994).
- <sup>39</sup>W. E. Vanderlinde and A. L. Ruoff, *J. Vac. Sci. Technol. B* **6**, 1621 (1988).
- <sup>40</sup>D. L. Flamm and V. M. Donnelly, *Plasma Chem. Plasma Process.* **1**, 317 (1981).
- <sup>41</sup>J. M. Cook and B. W. Benson, *J. Electrochem. Soc.* **130**, 2459 (1983).
- <sup>42</sup>G. S. Selwyn, *J. Appl. Phys.* **60**, 2771 (1986).
- <sup>43</sup>M. E. Harper, J. J. Cuomo, and H. R. Kaufman, *Annu. Rev. Mater. Sci.* **13**, 413 (1983).
- <sup>44</sup>F. D. Egitto, F. Emmi, R. S. Horwath, and V. Vukanovic, *J. Vac. Sci. Technol. B* **3**, 893 (1985).
- <sup>45</sup>O. Joubert, J. Pelletier, and Y. Arnal, *J. Appl. Phys.* **65**, 5096 (1989).
- <sup>46</sup>M. Schaepkens, T. E. F. M. Standaert, N. R. Rueger, P. G. M. Sebel, G. S. Oehrlein, and J. M. Cook, *J. Vac. Sci. Technol. A* **17**, 26 (1999).
- <sup>47</sup>P. F. Cheng, S. M. Rossnagel, and D. N. Ruzic, *J. Vac. Sci. Technol. B* **13**, 203 (1995).